MICROSCOPY

Spatiotemporal resolution in high-speed atomic force microscopy for studying biological macromolecules in action

Kenichi Umeda, Steven J. McArthur and Noriyuki Kodera [ID] *

Nano Life Science Institute (WPI-NanoLSI), Kanazawa University, Kakuma-machi, Kanazawa 920-1192, Japan
*To whom correspondence should be addressed. E-mail: nkodera@staff.kanazawa-u.ac.jp

Abstract

High-speed atomic force microscopy (HS-AFM) is a unique approach that allows direct real-time visualization of biological macromolecules in action under near-physiological conditions, without any chemical labeling. Typically, the temporal resolution is sub-100 ms, and the spatial resolution is 2–3 nm in the lateral direction and ∼0.1 nm in the vertical direction. A wide range of biomolecular systems and their dynamic processes have been studied by HS-AFM, providing deep mechanistic insights into how biomolecules function. However, the level of mechanistic detail gleaned from an HS-AFM experiment critically depends on the spatiotemporal resolution of the system. In this review article, we explain the principle of HS-AFM and describe how the resolution is determined. We also discuss recent attempts to improve the resolution of HS-AFM to further extend the observable range of biological phenomena.

Key words: atomic force microscopy, single-molecule imaging, biophysics, proteins, nucleic acids, biomolecules

Graphical abstract
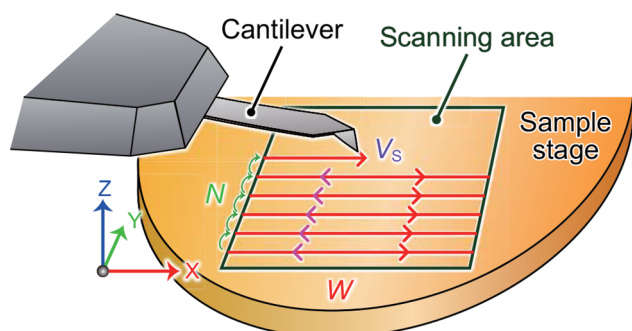
Introduction

Atomic force microscopy (AFM) is a palpation-type microscopy that creates three-dimensional maps of sample surfaces at a high spatial resolution by scanning a tiny probe tip attached to the end of a cantilever over a surface [1]. Since AFM measures the forces acting between the probe tip and the sample surface, AFM can observe a wide range of samples in various environments. Thus, AFM is now routinely used to characterize the topographies and mechanical properties of samples and continually pushes the frontiers of nanoscience and nanotechnology in physics, chemistry and biology [2–4].

AFM holds a unique significance in biological sciences because it is the only microscopy that can directly capture submolecular-resolution images of biological samples under near-physiological conditions without sample staining or chemical labeling [5–7]. In addition, AFM has been used for force measurements to estimate the strength of intra- and inter-molecular bonds at the single-molecule level [8–10] and the mechanical properties of living cells [11,12]. These applications have led AFM to become recognized as a multifunctional toolbox for biology [2]. However, the effective temporal resolution of conventional AFM is insufficient to capture dynamic behaviors of biological samples, requiring at least 30 s to obtain a single image. As a result, molecules moving on the substrate surface appear to be blurred or are not visible at all. This drawback had previously limited the application of AFM in functional studies of biological molecules.

To overcome this limitation, high-speed AFM (HS-AFM) for biological applications has been developed. After initial

prototyping [13,14] and extensive improvements [15–19], HS-AFM was first put into practical use around 2008 [20]. While the temporal resolution depends on the sample to be imaged and the imaging conditions, current HS-AFM systems can take successive images of biological samples ≤100 ms, allowing clear imaging of sub-100 ms molecular movements and dynamic processes. Importantly, despite the rapid pace of interactions between the probe tip and the sample, invasiveness is sufficiently low that the sample remains structurally and dynamically intact even after prolonged imaging.

Owing to the high speed and low invasiveness of HS-AFM, dynamic structural changes and functional processes in various biomolecular systems have been successfully imaged using HS-AFM, as reviewed previously [21–24]. In the past 3 years alone, numerous representative results have been reported on the following biomolecular systems: transmembrane proteins [25–30], peripheral membrane proteins [31–33], cytoskeletons and their binding proteins [34–38], nucleic acids and their binding proteins [39–52], intrinsically disordered proteins [53–57], molecular motors [58–61], amyloidogenic proteins [55,62–64], protein assemblies [65–68], membrane vesicles [69–71], disruption of cellular membrane [72–75], membraneless organelles [76,77] and artificial molecules [78–82]. The remarkable breadth of these achievements showcases the power of HS-AFM to open new avenues of investigation into diverse biomolecular systems and to obtain unique dynamic and mechanistic insights about these systems.

Although beyond the scope of this review, AFM operated in frequency modulation mode (FM-AFM) [83] has achieved atomic-scale imaging [84,85], atom manipulation [86,87] and chemical identification [88] for solid samples in ultra-high vacuum. Remarkably, true atomic-resolution imaging was demonstrated in liquid by FM-AFM [89,90], although applications toward biological molecules are still limited and the temporal resolution is not as high as that of HS-AFM [91–93]. The spatiotemporal resolution of FM-AFM is discussed in detail in previous studies [94–96].

In this review, we focus on HS-AFM for imaging biological macromolecules in action. First, we describe the principles underlying HS-AFM measurement and performance. Then, we explain the concept of the spatiotemporal resolution of HS-AFM. Finally, we discuss the recent attempts to improve the resolution of HS-AFM to extend its application range in the biological sciences.

Principle of HS-AFM

In brief, all AFM systems capture the topographies and physico-chemical properties of sample surfaces by scanning a probe tip attached to the free end of a microcantilever over a sample. While AFM can be performed in a number of operational modes [2], HS-AFM specifically employs the tapping mode, also called amplitude modulation mode or intermittent contact mode [97], which is usually used to observe fragile biological samples.

The system configuration of HS-AFM is basically the same as that of conventional tapping-mode AFM, but all components in the system are optimized for high-speed imaging (Fig. 1). In the tapping mode, the cantilever oscillates in the Z direction at around its first resonance frequency. When the cantilever approaches a sample surface, the oscillating probe tip intermittently taps the sample surface at the bottom of its swing. Hence, the oscillation amplitude
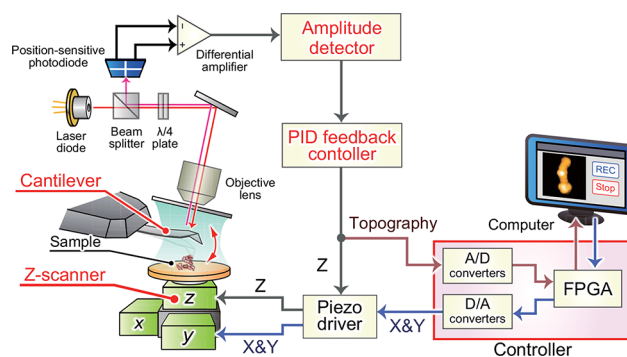
Fig. 1. Diagram of HS-AFM system.
HS-AFM, high-speed atomic force microscopy.

of the cantilever varies with the degree of contact. Using an optical beam deflection (OBD) system [98,99], the cantilever deflection is monitored by a laser beam reflected from the cantilever and guided to a position-sensitive photodiode. The output signals from the photodiode are conditioned to provide a differential signal corresponding to the cantilever deflection. The cantilever deflection signal is then converted to an amplitude signal by the amplitude detector. After that, the measured amplitude signal is compared with the preset amplitude values (i.e. the feedback set point amplitude), and their difference signal (i.e. the error signal) is fed into a proportional–integral–derivative (PID) feedback controller. The output signal from the feedback controller is fed into a Z piezo driver which displaces the Z-scanner, onto which the sample stage is affixed, in the Z direction so that the error signal approaches zero.

This series of operations is continuously repeated at different points on the sample surface during lateral scanning of the sample stage in the XY directions. The force acting between the probe tip and the sample surface is kept constant, minimizing the disruptive effect of the probe on the sample. The XY scanning signals are generated from a digital-to-analog (D/A) converter, and the output signal from the feedback controller at each XY position is recorded by an analog-to-digital (A/D) converter. This allows reconstruction of the topographic image of the sample surface. The temporal resolution of AFM is improved by decreasing the time required for each loop.

Feedback performance of HS-AFM

As mentioned earlier, two requirements must be met simultaneously to successfully apply HS-AFM to biological samples. One is temporal resolution high enough to capture the dynamic behavior of the sample, and the other is to minimize invasiveness in order to avoid disruption and deterioration of the sample. To this end, the following mechanical and electronic devices have been developed: small cantilevers with a small spring constant k_c and a high resonance frequency f_c [14,15], an OBD detection system using an objective lens specialized for small cantilevers [14], a high-speed amplitude detector [14], high-speed scanners [14,16,100], an active damper for the scanners [18], a dynamic PID feedback controller that outputs a large signal only when the probe tip is

detached from the sample surface [19] and a fast data acquisition system [17]. Details of these technical developments are described in previous studies [20,101].

The feedback system includes the cantilever, amplitude detector, PID feedback controller and Z-scanner (Fig. 1). The speed of the feedback control can be quantified by measuring the feedback bandwidth (f_B) in the closed loop system. Usually, f_B is defined by the feedback frequency at which a phase delay of $\pi/4$ occurs between the sample surface features to be observed (i.e. disturbance signal) and the Z-scanner displacement (i.e. feedback signal).

In reality, f_B is affected by various factors, including the ratio of the free oscillation amplitude of the cantilever A_0 and the sample height H_s, the ratio of A_0 and the feedback set point amplitude A_s and the physico-chemical properties of the sample and the tip–sample convolution [19,102,103] (Fig. 2). However, when H_s/A_0 and A_s/A_0 are small enough, f_B is well approximated by an open loop system using the sum of the time delays of the above devices as

$$f_B = \frac{1}{8} / \left(\tau_c + \tau_{amp} + \tau_z + \tau_d \right), \tag{1}$$

where τ_c, τ_{amp} and τ_z are the response time for the cantilever, amplitude detector and Z-scanner, respectively, and τ_d is the sum of the other small time delays in the feedback system. τ_c, τ_{amp}, and τ_z are further expressed by
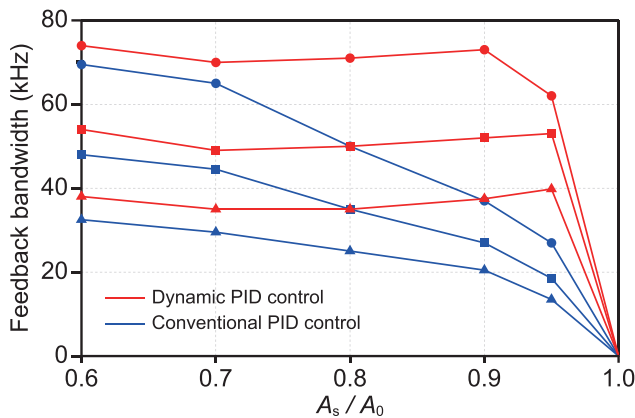
$$\tau_c = \frac{Q_c}{\pi f_c}, \tag{2}$$

$$\tau_{amp} = \frac{\Delta\varphi}{2\pi f_c} \tag{3}$$

and

$$\tau_z = \frac{Q_z}{\pi f_z}, \tag{4}$$

where f_c (f_z) and Q_c (Q_z) are the resonance frequency and the quality factor of the cantilever (Z-scanner), respectively, and

Fig. 2. Feedback bandwidth f_B is affected by various factors. f_B was measured by changing A_s/A_0 and A_0/H_s ratios using a mock AFM system [19]. Blue and red plots were obtained by conventional and dynamic PID controllers, respectively. Circle, square and triangle marks correspond to the A_0/H_s ratios of 5, 2 and 1, respectively [19].

AFM, atomic force microscopy; PID, proportional–integral–derivative.
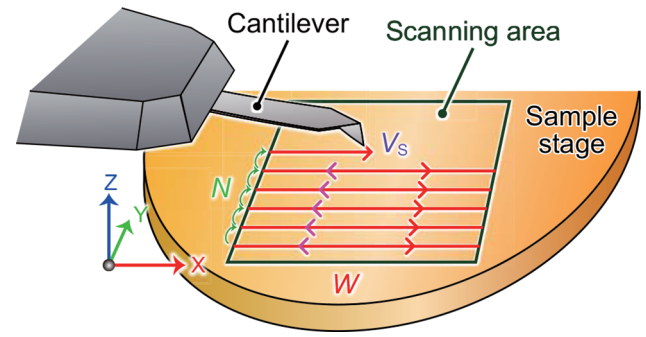
Fig. 3. Imaging parameters that determine the temporal resolution of AFM.

AFM, atomic force microscopy.

$\Delta\varphi$ is the phase delay in the amplitude detection with respect to the cantilever's oscillation cycle.

The current HS-AFM system achieves $f_B \sim 70$ kHz for low height samples [19], where τ_c is $\sim 0.4\,\mu s$ using a cantilever with $f_c \sim 1.2$ MHz and $Q_c \sim 1.5$ in liquid, τ_{amp} is $\sim 0.4\,\mu s$ using an amplitude detector with $\Delta\varphi \sim \pi$ [14] and a cantilever with $f_c \sim 1.2$ MHz, τ_z is $\sim 0.8\,\mu s$ using a Z-scanner with $f_z \sim 200$ kHz and $Q_z \sim 0.5$, and τ_d is $\sim 0.1\,\mu s$. The scanning area of HS-AFM for the observation of biological molecules in the XY and Z directions is $\sim 2 \times 2\,\mu m$ and $\sim 0.5\,\mu m$, respectively. In contrast, although the scanning area of conventional AFMs is much larger than HS-AFM, they typically have $f_B < 1$ kHz.

Temporal resolution of HS-AFM imaging

To consider the temporal resolution of HS-AFM, which we define as the minimum time to obtain an image T_{min}, we assume the XY-raster scanning method commonly used in biological applications (Fig. 3), notwithstanding non-raster scanning methods that have also been proposed [104,105]. When we suppose that an image is to be taken, given the smallest apparent width of features on the sample surface (σ), the scan range in the X direction (W) and the number of scanning lines in the Y direction (N), T_{min} is expressed by

$$T_{min} = \frac{\pi N W}{2\sigma\theta_{max}f_B}, \tag{5}$$

where θ_{max} (in radians) is the maximum possible phase delay in scanning the sample surface at which the resulting excess force exerted by the probe tip does not disturb the biological structure or function of the sample [106]. σ is approximated by the convolution of the probe tip radius R_t and the smallest sample feature radius to be observed R_s (i.e. $\sigma = \sqrt{R_t R_s}$).

In practice, the maximum scanning velocity of the probe tip V_{max} derived from T_{min} is a useful parameter for performing imaging experiments with optimized instrument performance. V_{max} is given by

$$V_{max} = \frac{2NW}{T_{min}}. \tag{6}$$

The line rate, which represents the X-scanning frequency, is another parameter that is often used to describe the imaging conditions of experiments. However, since the length of each X scan line varies depending on the size of the

scan area, it would be more useful to report the scanning velocity of the probe tip V_s, where V_s should be smaller than V_{max}. Since the efficiency of the feedback response is directly related to V_s, this allows the feedback response to be directly compared between studies regardless of the size of the scan area.

Although θ_{max} depends on the fragility of each target molecule, θ_{max} is estimated to be $\sim\pi/9$ (i.e. $\sim 20°$) for proteins, according to previous imaging studies [107]. Under a typical condition for imaging structural proteins (e.g. $W = 80$ nm, $N = 80$, $\sigma = 5$ nm, $f_B = 70$ kHz and $\theta_{max} = \pi/9$), V_{max} and T_{min} are estimated to be $\sim 150\,\mu$m/s and ~ 82 ms which corresponds to an imaging rate of ~ 12.2 frames per second (fps), respectively. Notably, some intrinsically disordered proteins with $\sigma \sim 2$ nm can be imaged without deterioration of their morphological and dynamic features for >2000 frames, even with an image acquisition time T of 20 ms (50 fps), with $W = 60$ nm, $N = 36$ and $f_B = 70$ kHz. This suggests that HS-AFM imaging can be performed even under conditions where θ_{max} probably exceeds $\pi/9$. This may be due to the substantially low height of intrinsically disordered regions, equivalent to the diameter of a single polypeptide chain (i.e. ~ 0.5 nm). Thus, higher temporal resolution imaging would be applicable to biological molecules with low height [108,109].

Importantly, Eq. (5) shows that the number of pixels in the X direction does not affect T_{min}: that is, putting a large number of pixels in the X direction does not result in a decrease in temporal resolution. Indeed, some imaging studies skillfully used this idea to collect more information from the sample surface by using a rectangular pixel, with a smaller pixel size and a higher pixel count in the X direction [72,110,111]. Furthermore, Eq. (5) implies that the temporal resolution of AFM can be increased by decreasing N, as demonstrated previously [35,112,113]. More specifically, line scanning mode ($N = 1$) provides a temporal resolution as short as a few tenths of the time needed to capture a full image [13,114]. This approach has been demonstrated in the successful quantification of the fast kinetics of membrane proteins [115–117]. At the extreme, it is also possible to follow the height change at a certain fixed position on a sample [118,119]. Indeed, oligomeric states and concentrations of a membrane binding molecule on a biological model membrane have been studied by HS-AFM in this way at a temporal resolution of $\sim 10\,\mu$s [115].

Spatial resolution of HS-AFM imaging

Since AFM topographic images depict the height variation in the Z direction as a function of the spatial coordinates in the XY plane, the spatial resolution must be separated into vertical (Z) and lateral (XY) resolution. These are affected by various factors: mechanical and electrical noise from the instrument, the size and shape of the probe tip, the forces acting between the probe tip and sample, the physico-chemical properties of the sample and so on [120]. Biological samples in particular need additional considerations because they have viscoelastic properties and are highly dynamic in nature, exhibiting thermal fluctuation and functional movements; these will be discussed later. However, for simplicity, we will first consider the case where the deformations and movements of the sample can be ignored.

The vertical resolution δZ is determined by the thermal noise of the cantilever δZ_{th}, the noise of the OBD sensor δZ_{det}

and the noise of the Z-scanner δZ_s, when the cantilever is oscillated at or near its first resonance frequency. As these noise sources are independent, δZ is given as

$$\delta Z = \sqrt{\delta Z_{th}{}^2 + \delta Z_{det}{}^2 + \delta Z_s{}^2}. \qquad (7)$$

Since δZ_{det} and δZ_s are negligible compared to δZ_{th} in the HS-AFM system, Eq. (7) can be approximated as

$$\delta Z \cong \sqrt{\frac{4k_B T_{exp} Q_c f_B}{\pi f_c k_c}} \qquad (8)$$

where k_B and T_{exp} are the Boltzmann constant and the temperature in Kelvin during the experiment, respectively [121]. δZ_{th} is estimated to be ~ 0.05 nm in our HS-AFM system under typical parameters (i.e. $f_c = 1.2$ MHz, $k_c = 0.2$ N/m, $Q_c = 1.5$, $f_B = 70$ kHz and $T_{exp} = 298$ K). This is a sufficient vertical resolution to observe the 0.34-nm layer-to-layer step height of highly oriented pyrolytic graphite, corresponding to the average size of amino acids [54].

The lateral resolution is considered using the Rayleigh criterion and is predominantly determined by the shape of the probe tip [122]. As shown in Fig. 4a, a pair of sharp spikes, with a height difference Δh, separated by distance l is scanned by a probe with a tip radius R_t. As the samples are considerably sharper than the tip, the resulting topographic image shows a pair of inverted probe tips intersecting the top of the spikes. The intersection of the shapes of the inverted probe tips forms a small dimple with depth ΔZ. The lateral resolution δl can be determined by the minimum lateral separation l for which ΔZ is larger than the vertical resolution of the system, δZ. Therefore, δl can be approximated as

$$\delta l \cong \sqrt{2R_t}\left(\sqrt{\delta Z} + \sqrt{\delta Z + \Delta h}\right), \qquad (11)$$

for $\delta l > \sqrt{2R_t \Delta h}$, where ΔZ and Δh are finite quantities, and thus their multiplications can be ignored. Figure 4b shows the lateral resolution as a function of R_t using δZ of 0.05 nm as estimated earlier. When samples have no height difference, δl of ~ 1.5 nm can be achieved with a probe of $R_t \sim 5$ nm. By contrast, in a realistically observable case where samples have a height difference of only ~ 1 nm, δl increases to 3–4 nm using the same probe tip of $R_t \sim 5$ nm. These probe tips can be fabricated at the end of a cantilever using electron beam deposition followed by argon plasma etching [22]. In good cases, δl as low as ~ 1 nm can be achieved for samples with low height differences [29,109], implying that probe tips can be fabricated using this procedure with R_t as low as 1–2 nm.

Since AFM images are digital data, the spatial resolution is also affected by the data acquisition process. According to the sampling theorem, the size of a single image pixel should be less than half of the desired resolution. The A/D and D/A converters used in our current HS-AFM system are 12 bits for ± 1 V (PCI-3525 and PCI-3305, Interface, Japan) corresponding to minimum digital resolutions of ~ 0.10 nm and ~ 0.03 nm in the XY and Z directions, respectively. While the minimum digital resolutions depend on the maximum displacements of the scanner, they are smaller than the lateral and vertical resolutions of the instrument.

In principle, AFM generates accurate and reliable height information relative to a reference plane. However, as
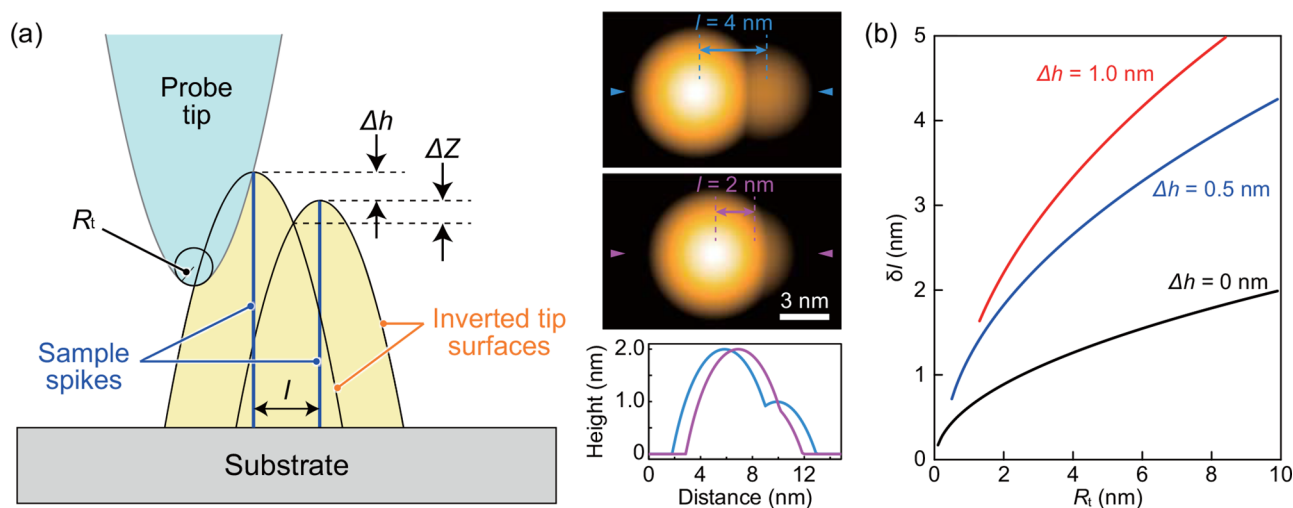
Fig. 4. Estimation of lateral spatial resolution of AFM based on a simple geometric configuration. (a) Left, AFM image reconstruction based on the Rayleigh criterion. Two sample spikes are scanned by a parabolic probe tip with radius R_t. Modified based on ref [122]. Right, pseudo AFM images for the two spikes (top and center) and their cross-sections (bottom). The two spikes, separated by 4 nm (top) and 2 nm (center), are scanned by a probe tip with R_t of 5 nm. The height difference Δh of the spikes is 1 nm. Cross-sections are along the axis denoted by the arrowheads, which passes through the peaks. (b) Lateral resolution of HS-AFM δl as a function of R_t for two adjacent features, assuming δZ of 0.05 nm. Modified based on ref [120].

AFM, atomic force microscopy; HS-AFM, high-speed atomic force microscopy.

mentioned earlier, the width and volume of an imaged object should be carefully quantified because AFM images are acquired with a convolution effect caused by the tip scanning [123]; this effect is especially pronounced for biological molecules whose size is comparable to R_t. In addition, when observing objects with sizes similar to R_t, a multi-tip effect often appears in images [124]. Both effects must be taken into account when analyzing and interpreting width and volume data obtained by AFM.

Remarkably, to overcome the limit on AFM spatial resolution imposed by the tip convolution effect, a method called the localization image reconstruction algorithm [125] was developed based on the localization microscopy technique that has revolutionized the spatial resolution of fluorescence microscopy [126,127]. This method has since been applied to demonstrate that single amino acid residues on membrane proteins in native and dynamic conditions can be resolved by AFM [29,117,125].

Apparent spatial resolution and data asynchronicity

Next, we consider the case where the sample deforms and moves during AFM imaging. It is important to consider that the data for all pixels in an image are not acquired at the same time, but at different times during the lateral scanning of the sample stage; this is called data asynchronicity. Accordingly, one can easily imagine that a slow scan of a fast-moving object would result in a blurred image of the object, resulting in low spatial resolution [128,129]. Biological molecules exhibit translational diffusion, rotational diffusion and conformational changes related to their functions, all of which affect the appearance of observed objects (Fig. 5) and therefore the apparent spatial resolution of the AFM image. Thus, improving the temporal resolution of AFM is key to observing dynamic and mobile biological molecules and clearly resolving their detailed features.

This concept is demonstrated by a study that includes HS-AFM imaging of an intrinsically disordered protein. It was

demonstrated that the disordered regions are not visible at 1 fps, only slightly visible at 2 fps, visible with their end regions appearing blurry at 5 fps and clearly visible for the entire length at 10 fps [130]. Indeed, using a high temporal resolution to obtain a high apparent spatial resolution, HS-AFM has been used to determine the stoichiometry of protein complexes that have not been determined by other methods [35,131–134]. Thus, improving the temporal resolution of AFM concomitantly improves the apparent spatial resolution of images.

Further improvements of HS-AFM

The power of HS-AFM has been progressively demonstrated by imaging studies on various targets as mentioned earlier. However, there are still a large number of biological processes that cannot be visualized with current HS-AFM systems. This is largely due to the insufficient temporal resolution of HS-AFM. For example, typical enzymatic reactions take place on a time scale shorter than ~10 ms. However, with a T_{min} of ~80 ms estimated by Eq. (5) under typical imaging conditions ($W = 50$ nm, $N = 50$, $\sigma = 2$ nm, $f_B = 70$ kHz and $\theta_{max} = \pi/9$), HS-AFM only captures ~0.1% of the enzymatic reactions taking place; the remaining ~99.9% will have completed in the time it takes to acquire a single image (Fig. 6a). In addition, while there are numerous membrane proteins that diffuse on the surface of eukaryotic cells, they have not been observed by AFM at all. This is due to the relationship between the diffusion constant of membrane proteins on the cellular membrane ($D_{2D} \sim 0.1$ μm^2/s) [135] and the low temporal resolution $T_{min} \sim 2.6$ s under typical imaging conditions for living cells ($W = 1000$ nm, $N = 200$, $\sigma = 5$ nm, $f_B = 70$ kHz and $\theta_{max} = \pi/9$). About half of the molecules of interest diffuse out of the observation area while taking an image (Fig. 6b), making it impossible to identify and track the same molecule in subsequent images.

Therefore, further improvement of the temporal resolution of HS-AFM is a key stepping stone toward visualizing a wider
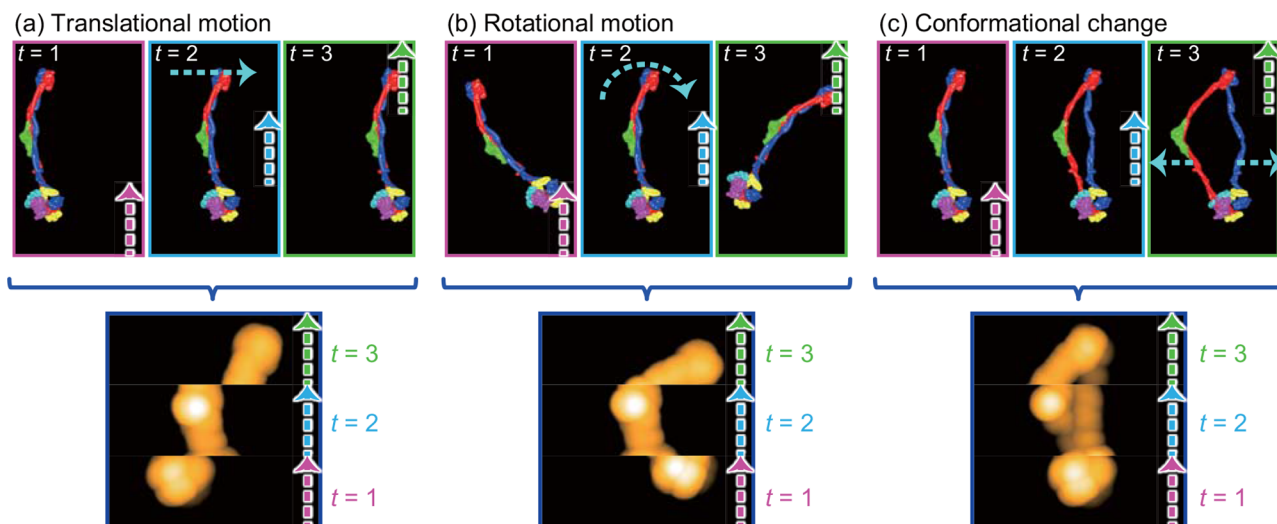
Fig. 5. Effect of data asynchronicity on AFM imaging for a mobile sample. (a) Translational motion, (b) rotational motion and (c) conformational change of a molecule of SMC5/6 complex over time ($t = 1, 2, 3$). The thick dashed lines represent the progress of the scan whereas the thin dashed lines represent the protein movements. The upper and lower panels show the shape of the molecule at each time and the single AFM images taken over t from 0 to 3, respectively. The AFM images are pseudo AFM images based on the Protein Data Bank structure (PDB 7QCD), generated using an AFM simulator.

AFM, atomic force microscopy.

range of biological phenomena. As mentioned previously, the speed performance of AFM is determined by f_B, which is correlated to the sum of the response times of the devices contained in the feedback loop for maintaining the tip–sample interaction force (Fig. 6c). To substantially increase f_B, all devices need to be improved. Here, we summarize recent efforts to that end.

First, we developed a new Z-scanner named 'Z-scanner speed-booster' (Z-SB) with f_z >1.1 MHz, corresponding to τ_z of ~0.14 µs (Fig. 6d and e) [136]. In the mechanical design, a small piezo actuator is supported at its bottom four vertices on a cone-like hollow (Fig. 6d), allowing f_z to remain as high as that of the piezo actuator in free vibration. As Z-SB is light and compact, it can be integrated to improve the performance of a sample-scanning AFM system without modifying the original Z-scanner (Fig. 6e right). By combining Z-SB with the dual Z-scanner system [137,138], short timescale dynamic molecular events occurring on the surfaces of organelles and cells can be imaged with higher temporal resolution.

Regarding the amplitude detector, the sample-and-hold-based method with $\Delta\varphi$ of π (i.e. 180°) used to be the fastest type [14]. To reduce $\Delta\varphi$, Miyagi and Scheuring introduced a novel analog amplitude detector based on trigonometric calculation [139], in which a phase shifter was used to obtain a signal with a phase delay of 90° from the input signal: this is known as the phase-shift based (PSB) method. Theoretically, a PSB detector is expected to reach $\Delta\varphi$ of 30°. However, due to the circuit latency, the actual $\Delta\varphi$ was ~138° at f_c of 0.5 MHz, which corresponds to τ_{amp} of ~0.77 µs.

To further reduce $\Delta\varphi$, we developed a new amplitude detector using a differential-based (DB) detection algorithm (Fig. 6f) [140], which theoretically has no intrinsic latency, by modifying the PSB algorithm. As this detector generates squared amplitude (A^2), we call this detector DB-A^2. Although true zero latency performance could not be observed experimentally due to the analog circuit latency, we found that at f_c < 1 MHz, the detector bandwidth surpassed f_c

(corresponding to the 45° line) and even the theoretical PSB bandwidth of the 30° line (Fig. 6g). At f_c of 0.5 MHz, $\Delta\varphi$ is calculated to be ~20°, corresponding to τ_{amp} of ~0.11 µs. The square root operation needed in conventional amplitude detectors was determined to be a significant bottleneck (Fig. 6g). In addition to the speed advantage incurred by eliminating the square root operation, the use of the A^2 signal makes the amplitude distance dependence steeper, which contributes to reducing the invasiveness of AFM imaging (see the supplemental material in ref [140]). Finally, by employing faster operational amplifiers, the detector bandwidth could be further improved to at least 2 MHz corresponding to τ_{amp} of ~0.06 µs independent of f_c.

The remaining challenge is to speed up the cantilever. To achieve higher f_c while keeping k_c as small as the current model (~0.2 N/m), further miniaturization of the cantilever is required. Our preliminary experiment suggests that the deflection signal of a cantilever with a length of 2 µm and a width of 0.75 µm can be measured using the current OBD detection system with a slight modification. If the thickness could be reduced to 50 nm, it would be possible to realize an ultra-small cantilever with f_c of ~4.5 MHz in liquid and k_c of ~0.2 N/m whose τ_c corresponds to ~0.11 µs assuming Q_c of 1.5.

Successfully combining these improvements could yield an HS-AFM system with a 4-fold improved f_B of ~300 kHz for low height samples (Fig. 6c), assuming the following parameters: τ_c of ~0.11 µs using a cantilever with $f_c \sim 4.5$ MHz and $Q_c \sim 1.5$ in liquid, τ_{amp} of ~0.06 µs using an advanced DB-A^2, τ_z of ~0.14 µs using Z-SB with $f_z \sim 1.1$ MHz and $Q_z \sim 0.5$, and τ_d of ~0.1 µs.

Another opportunity for optimization was found in the relative movement of the tip during scanning. Retrace imaging during backward X-scanning as the tip returns to the start of each scan line produces larger feedback error than trace imaging (i.e. forward X-scanning) because of the different torques exerted on the probe tip by the sample. In light of this, the only-trace-imaging (OTI) mode, which eliminates the
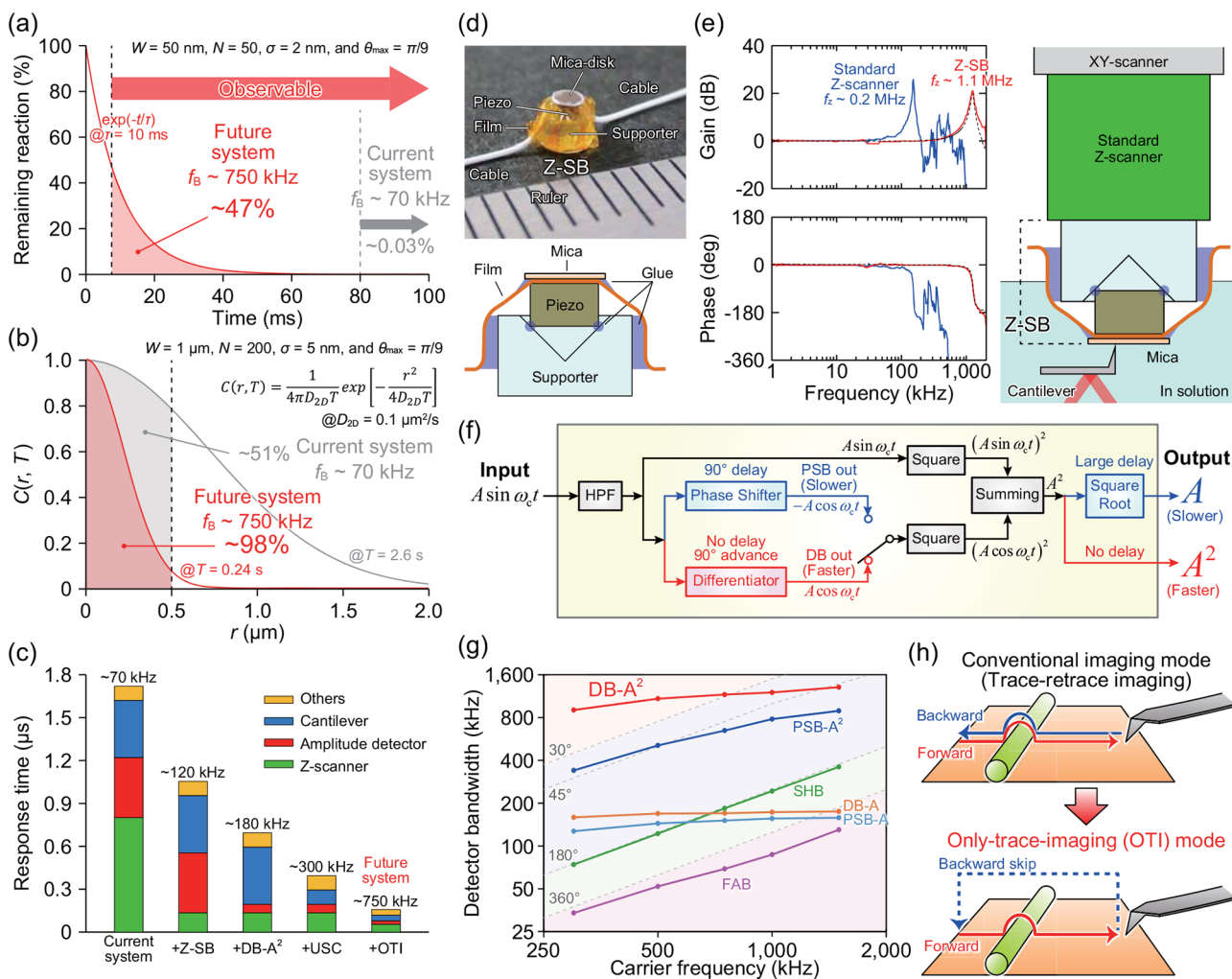
Fig. 6. Current efforts to improve the temporal resolution of HS-AFM. (a) Relationship between an enzymatic reaction and the temporal resolution of current and future HS-AFM. The enzymatic reaction was assumed to be a first-order reaction with a time constant of 10 ms. (b) Relationship between the 2D diffusion of a membrane protein on living cells and the temporal resolution of current and future HS-AFM. The probability $C(r, T)$ represents whether a molecule diffusing on a 2D plane remains in a given observation area of radius r after a given time T. (c) Summary of response time and feedback bandwidth of various HS-AFM systems. (d) Picture (top) and schematic (bottom) of Z-SB [136]. (e) Left, comparison between the frequency responses of the standard Z-scanner (blue) and Z-SB (red). Right, schematic showing how to install the Z-SB into an HS-AFM system. The Z-SB is attached onto the top of a standard Z-scanner [136]. (f) Circuit diagram of DB and PSB amplitude detector [140]. (g) Detector bandwidth of various amplitude detectors [140]. (h) Comparison between the conventional imaging (trace–retrace imaging) mode and the OTI mode [141].

2D, two-dimensional; DB, differential-based; USC, ultra-small cantilever; HS-AFM, high-speed atomic force microscopy; OTI, only-trace-imaging; PSB, phase-shift-based; Z-SB, Z-scanner speed-booster; FAB, Fourier analysis–based detector.

retrace scan by lifting the tip away from the surface during the retrace, was introduced (Fig. 6h) [141]. Surprisingly, the OTI mode was found to improve T_{min} by up to ~2.5-fold compared to the conventional trace–retrace imaging mode because the elimination of the retrace scan allows the tip to return to the start of the line at higher speeds, while simultaneously reducing the tip–sample contact time and thereby reducing the invasiveness of AFM imaging. The effective feedback bandwidth of an optimized HS-AFM system with a f_B of ~300 kHz could therefore be increased as high as ~750 kHz through the use of OTI mode imaging, an improvement of >10-fold over the current HS-AFM systems (Fig. 6c). This improved temporal resolution of HS-AFM would greatly expand the range of observable biological phenomena (Fig. 6a and b). Implementing the OTI mode requires minor modifications

to the software for operating AFM and an extra D/A board that generates a false amplitude signal during the retrace scan [141].

Continuous efforts to improve the spatiotemporal resolution of HS-AFM are necessary. However, the issue of data asynchronicity is inherent in AFM imaging and cannot be eliminated in principle. Other inherent limitations to AFM imaging include the tip convolution effect and the fact that the inside of the sample cannot be observed at all. Remarkably, different groups are beginning to use the methods of computational science and data science to address these issues. By simulating a pseudo AFM image using the atomically resolved structural information of a biological molecule, the correlation between the experimental AFM image and the theoretical model can be analyzed, providing insight into the

molecule's internal structure [16,142–146]. In addition, a sequential Bayesian data assimilation approach was adopted to address the issue of data asynchronicity in AFM [147–150]. This approach reduced image distortion and noise caused by data asynchronicity [147] and demonstrated that the detailed behaviors of biological molecules including their interiors can be analyzed far beyond the limits defined by the spatiotemporal resolution of HS-AFM [148–150]. Moreover, a method based on a modern machine learning approach was recently developed to remove the tip convolution effect as well as the multi-tip effect [151]. These computational methods could play an important role in extracting additional useful information from HS-AFM data.

Concluding remarks

Recent advances in structural biology have yielded numerous beautiful albeit static structures at atomic resolution [152]. In addition, time-resolved X-ray crystallography and cryo-electron microscopy have been applied to resolve structures over a time course [153–155]. However, the data are not gathered in real time and consist of ensemble averaged structures encompassing many classes of conformations. In contrast, HS-AFM can visualize the structural changes that occur in a single molecule in real time and real space, allowing a deeper and more direct understanding of the functional mechanism of biological molecules. Therefore, HS-AFM continues to play an important and unique role as a technique in structural biology even given the current limits to its spatiotemporal resolution. HS-AFM remains an advantageous technique for studying heterogeneous, highly fluctuating biological samples; moreover, ongoing development of the microscope components and improvements in spatiotemporal resolution promise to expand the range of observable phenomena. Further innovations, including real-time temperature control [156,157], force modulation [158,159], uneven substrates [33,160] and tip-scanning HS-AFM combined with fluorescence microscopy [161,162], promise to open even more frontiers in single-molecule biology.

Here, we describe how the spatiotemporal resolution of HS-AFM is determined. As with any experimental technique, it is important to be familiar with the principle and methods for assessing performance in order to obtain and interpret high-quality data. We hope that this review will serve to further stimulate the study of biological molecules by HS-AFM.

References

1. Binnig G et al (1986) Atomic force microscope. *Phys. Rev. Lett.* 56: 930–933.
2. Dufrêne Y F et al (2017) Imaging modes of atomic force microscopy for application in molecular and cell biology. *Nat. Nanotechnol.* 12: 295–307.
3. Gross L et al (2018) Atomic force microscopy for molecular structure elucidation. *Angew. Chem. Int. Ed.* 57: 3888–3908.
4. Garcia R (2020) Nanomechanical mapping of soft materials with the atomic force microscope: methods, theory and applications. *Chem. Soc. Rev.* 49: 5850–5884.
5. Drake B et al (1989) Imaging crystals, polymers, and processes in water with the atomic force microscope. *Science* 243: 1586–1589.
6. Henderson E et al (1992) Actin filament dynamics in living glial cells imaged by atomic force microscopy. *Science* 257: 1944–1946.
7. Hörber J K H and Miles M J (2003) Scanning probe evolution in biology. *Science* 302: 1002–1005.
8. Florin E-L et al (1994) Adhesion forces between individual ligand-receptor pairs. *Science* 264: 415–417.
9. Allison D P et al (2002) Biomolecular force measurements and the atomic force microscope. *Curr. Opin. Biotechnol.* 13: 47–51.
10. Hinterdorfer P and Dufrêne Y F (2006) Detection and localization of single molecular recognition events using atomic force microscopy. *Nat. Methods* 3: 347–355.
11. Efremov Y M et al (2020) Measuring viscoelasticity of soft biological samples using atomic force microscopy. *Soft Matter* 16: 64–81.
12. Müller D J et al (2021) Atomic force microscopy-based force spectroscopy and multiparametric imaging of biomolecular and cellular systems. *Chem. Rev.* 121: 11701–11725.
13. Viani M B et al (2000) Probing protein–protein interactions in real time. *Nat. Struct. Biol.* 7: 644–647.
14. Ando T et al (2001) A high-speed atomic force microscope for studying biological macromolecules. *Proc. Natl. Acad. Sci. USA* 98: 12468–12472.
15. Kitazawa M et al (2003) Batch fabrication of sharpened silicon nitride tips. *Jpn. J. Appl. Phys.* 42: 4844–4847.
16. Ando T et al (2005) High-speed atomic force microscopy for capturing dynamic behavior of protein molecules at work. *e-JSSNT* 3: 384–392.
17. Fantner G E et al (2005) Data acquisition system for high speed atomic force microscopy. *Rev. Sci. Instrum.* 76: 026118.
18. Kodera N et al (2005) Active damping of the scanner for high-speed atomic force microscopy. *Rev. Sci. Instrum.* 76: 053708.
19. Kodera N et al (2006) Dynamic proportional-integral-differential controller for high-speed atomic force microscopy. *Rev. Sci. Instrum.* 77: 083704.
20. Ando T et al (2008) High-speed atomic force microscopy for nano-visualization of dynamic biomolecular processes. *Prog. Surf. Sci.* 83: 337–437.
21. Katan A J and Dekker C (2011) High-speed AFM reveals the dynamics of single biomolecules at the nanometer scale. *Cell* 147: 979–982.
22. Ando T et al (2014) Filming biomolecular processes by high-speed atomic force microscopy. *Chem. Rev.* 114: 3120–3188.
23. Heath G R and Scheuring S (2019) Advances in high-speed atomic force microscopy (HS-AFM) reveal dynamics of transmembrane channels and transporters. *Curr. Opin. Struct. Biol.* 57: 93–102.
24. Ando T; (2019) High-speed atomic force microscopy. *Curr. Opin. Chem. Biol.* 51: 105–112.
25. Kawasaki Y et al (2020) Two-state exchange dynamics in membrane-embedded oligosaccharyltransferase observed in real-time by high-speed AFM. *J. Mol. Biol.* 432: 5951–5965.
26. Lin Y C et al (2020) Annexin-V stabilizes membrane defects by inducing lipid phase transition. *Nat. Commun.* 11: 230.

27. Tokano T et al (2020) Structural dynamics of a protein domain relevant to the water-oxidizing complex in photosystem II as visualized by high-speed atomic force microscopy. *J. Phys. Chem. B* 124: 5847–5857.

28. Jiao F et al (2022) Perforin-2 clockwise hand-over-hand pre-pore to pore transition mechanism. *Nat. Commun.* 13: 5039.

29. Jiang Y et al (2022) Membrane-mediated protein interactions drive membrane protein organization. *Nat. Commun.* 13: 7373.

30. Nishiguchi S et al (2022) Multiple dimeric structures and strand-swap dimerization of E-cadherin in solution visualized by high-speed atomic force microscopy. *Proc. Natl. Acad. Sci. USA* 119: e2208067119.

31. Bertin A et al (2020) Human ESCRT-III polymers assemble on positively curved membranes and induce helical membrane tube formation. *Nat. Commun.* 11: 2663.

32. Jiao F et al (2020) The hierarchical assembly of septins revealed by high-speed AFM. *Nat. Commun.* 11: 5062.

33. Jukic N et al (2022) Snf7 spirals sense and alter membrane curvature. *Nat. Commun.* 13: 2174.

34. Matsuda K et al (2020) Visualizing dynamic actin cross-linking processes driven by the actin-binding protein anillin. *FEBS Lett.* 594: 1237–1247.

35. Kodera N et al (2021) Native cyclase-associated protein and actin from *Xenopus laevis* oocytes form a unique 4:4 complex with a tripartite structure. *J. Biol. Chem.* 296: 100649.

36. Fujita J et al (2021) Dynamic assembly/disassembly of *Staphylococcus aureus* FtsZ visualized by high-speed atomic force microscopy. *Int. J. Mol. Sci.* 22: 1697.

37. Nasrin S R et al (2021) Deformation of microtubules regulates translocation dynamics of kinesin. *Sci. Adv.* 7: eabf2211.

38. Moretto L et al (2022) Multistep orthophosphate release tunes actomyosin energy transduction. *Nat. Commun.* 13: 4575.

39. Feng Y et al (2020) Direct observation of dynamic interactions between orientation-controlled nucleosomes in a DNA origami frame. *Chem. Eur. J.* 26: 15282–15289.

40. Pan Y et al (2020) High-speed atomic force microscopy directly visualizes conformational dynamics of the HIV Vif protein in complex with three host proteins. *J. Biol. Chem.* 295: 11995–12001.

41. Ryu J K et al (2020) The condensin holocomplex cycles dynamically between open and collapsed states. *Nat. Struct. Mol. Biol.* 27: 1134–1141.

42. Tatebe H et al (2020) Rad50 zinc hook functions as a constitutive dimerization module interchangeable with SMC hinge. *Nat. Commun.* 11: 370.

43. Xing X et al (2020) Direct observation and analysis of TET-mediated oxidation processes in a DNA origami nanochip. *Nucleic Acids Res.* 48: 4041–4051.

44. Bauer B W et al (2021) Cohesin mediates DNA loop extrusion by a "swing and clamp" mechanism. *Cell* 184: 5448–5464.e5422.

45. Hirano R et al (2021) Histone variant H2A.B-H2B dimers are spontaneously exchanged with canonical H2A-H2B in the nucleosome. *Commun. Biol.* 4: 191.

46. Nakano M et al (2021) Ultrastructure of influenza virus ribonucleoprotein complexes during viral RNA synthesis. *Commun. Biol.* 4: 858.

47. Sethi S et al (2021) Non-invasive regulation of cellular morphology using a photoswitchable mechanical DNA polymer. *Angew. Chem. Int. Ed.* 60: 20342–20349.

48. Sun Z et al (2021) Dynamics of the PriA helicase at stalled DNA replication forks. *J. Phys. Chem. B* 125: 4299–4307.

49. Vemulapalli S et al (2021) Site-search process for synaptic protein-DNA complexes. *Int. J. Mol. Sci.* 23: 212.

50. Sun Z et al (2022) Three-way DNA junction as an end label for DNA in atomic force microscopy studies. *Int. J. Mol. Sci.* 23: 11404.

51. Tsuji A et al (2022) Dimerization processes for light-regulated transcription factor Photozipper visualized by high-speed atomic force microscopy. *Sci. Rep.* 12: 12903.

52. Yoshimi K et al (2022) Dynamic mechanisms of CRISPR interference by *Escherichia coli* CRISPR-Cas3. *Nat. Commun.* 13: 4917.

53. Imai H et al (2020) Direct visualization of translational GTPase factor pool formed around the archaeal ribosomal P-stalk by high-speed AFM. *Proc. Natl. Acad. Sci. USA.* 117: 32386–32394.

54. Kodera N et al (2021) Structural and dynamics analysis of intrinsically disordered proteins by high-speed atomic force microscopy. *Nat. Nanotechnol.* 16: 181–189.

55. Konno H et al (2020) Dynamics of oligomer and amyloid fibril formation by yeast prion Sup35 observed by high-speed atomic force microscopy. *Proc. Natl. Acad. Sci. USA* 117: 7831–7836.

56. Sakane A et al (2021) JRAB/MICAL-L2 undergoes liquid-liquid phase separation to form tubular recycling endosomes. *Commun. Biol.* 4: 551.

57. Matsuo Y et al (2023) Decoding of the ubiquitin code for clearance of colliding ribosomes by the RQT complex. *Nat. Commun.* 14: 79.

58. Qu M et al (2020) High-speed atomic force microscopy reveals factors affecting the processivity of chitinases during interfacial enzymatic hydrolysis of crystalline chitin. *ACS Catal.* 10: 13606–13615.

59. Kobayashi K et al (2021) Movements of mycoplasma mobile gliding machinery detected by high-speed atomic force microscopy. *mBio* 12: e0004021.

60. Toyonaga T et al (2021) Chained structure of dimeric F(1)-like ATPase in mycoplasma mobile gliding machinery. *mBio* 12: e0141421.

61. Uchiyama T et al (2022) Lytic polysaccharide monooxygenase increases cellobiohydrolases activity by promoting decrystallization of cellulose surface. *Sci. Adv.* 8: eade5155.

62. Watanabe-Nakayama T et al (2020) Self- and cross-seeding on alpha-synuclein fibril growth kinetics and structure observed by high-speed atomic force microscopy. *ACS Nano* 14: 9979–9989.

63. Beton J G et al (2022) Cooperative amyloid fibre binding and disassembly by the Hsp70 disaggregase. *EMBO J.* 41: e110410.

64. Sahoo B R et al (2022) Conformational tuning of amylin by charged styrene-maleic-acid copolymers. *J. Mol. Biol* 434: 167385.

65. Strasser J et al (2020) Weak fragment crystallizable (Fc) domain interactions drive the dynamic assembly of IgG oligomers upon antigen recognition. *ACS Nano.* 14: 2739–2750.

66. Valbuena A et al (2020) Visualization of single molecules building a viral capsid protein lattice through stochastic pathways. *ACS Nano.* 14: 8724–8734.

67. Hatzopoulos G N et al (2021) Tuning SAS-6 architecture with monobodies impairs distinct steps of centriole assembly. *Nat. Commun.* 12: 3805.

68. Yagi-Utsumi M et al (2021) Desiccation-induced fibrous condensation of CAHS protein from an anhydrobiotic tardigrade. *Sci. Rep.* 11: 21328.

69. Kikuchi Y et al (2020) Diversity of physical properties of bacterial extracellular membrane vesicles revealed through atomic force microscopy phase imaging. *Nanoscale* 12: 7950–7959.

70. Sajidah E S et al (2022) Spatiotemporal tracking of small extracellular vesicle nanotopology in response to physicochemical stresses revealed by HS-AFM. *J. Extracell. Vesicles* 11: 12275.

71. Yamaguchi H et al (2022) Extracellular vesicles contribute to the metabolism of transthyretin amyloid in hereditary transthyretin amyloidosis. *Front. Mol. Biosci.* 9: 839917.

72. Zuttion F et al (2020) High-speed atomic force microscopy highlights new molecular mechanism of daptomycin action. *Nat. Commun.* 11: 6312.

73. Yamamura H et al (2021) Antibacterial activity of membrane-permeabilizing bactericidal cyclodextrin derivatives. *ACS Omega* 6: 31831–31842.

74. Ngo K X et al (2022) Unraveling the host-selective toxic inter-action of cassiicolin with lipid membranes and its cytotoxicity. *Phytopathology* 112: 1524–1536.

75. Shukla R et al (2022) Teixobactin kills bacteria by a two-pronged attack on the cell envelope. *Nature* 608: 390–396.

76. Fujioka Y et al (2020) Phase separation organizes the site of autophagosome formation. *Nature* 578: 301–305.

77. Yamasaki A et al (2020) Liquidity is a critical determinant for selective autophagy of protein condensates. *Mol. Cell* 77: 1163–1175.e1169.

78. Maity S et al (2020) Caught in the act: mechanistic insight into supramolecular polymerization-driven self-replication from real-time visualization. *J. Am. Chem. Soc.* 142: 13709–13717.

79. Kikuchi K et al (2022) Protein needles designed to self-assemble through needle tip engineering. *Small* 18: 2106401.

80. Ueno T et al (2020) Dynamic behavior of an artificial protein nee-dle contacting a membrane observed by high-speed atomic force microscopy. *Nanoscale* 12: 8166–8173.

81. Sharma M et al (2022) Shape-morphing of an artificial pro-tein cage with unusual geometry induced by a single amino acid change. *ACS Nanosci. Au* 2: 404–413.

82. Majsterkiewicz K et al (2022) Artificial protein cage with unusual geometry and regularly embedded gold nanoparticles. *Nano Lett.* 22: 3187–3195.

83. Albrecht T R et al (1991) Frequency modulation detection using high-Q cantilevers for enhanced force microscope sensitivity. *J. Appl. Phys.* 69: 668–673.

84. Giessibl F J (1995) Atomic-resolution of the silicon (111)-(7x7) surface by atomic-force microscopy. *Science* 267: 68–71.

85. Giessibl F J et al (2000) Subatomic features on the silicon (111)-(7×7) surface observed by atomic force microscopy. *Science* 289: 422–425.

86. Sugimoto Y et al (2005) Atom inlays performed at room temper-ature using atomic force microscopy. *Nat. Mater.* 4: 156–159.

87. Sugimoto Y et al (2007) Chemical identification of individual surface atoms by atomic force microscopy. *Nature* 446: 64–67.

88. Sugimoto Y et al (2008) Complex patterning by vertical inter-change atom manipulation using atomic force microscopy. *Science* 322: 413–417.

89. Fukuma T et al (2005) True atomic resolution in liquid by frequency-modulation atomic force microscopy. *Appl. Phys. Lett.* 87: 034101.

90. Hoogenboom B W et al (2006) Quantitative dynamic-mode scanning force microscopy in liquid. *Appl. Phys. Lett.* 88: 193109.

91. Asakawa H et al (2011) Submolecular-scale imaging of α-Helices and C-Terminal domains of tubulins by frequency modulation atomic force microscopy in liquid. *Biophys. J.* 101: 1270–1276.

92. Leung C et al (2012) Atomic force microscopy with nanoscale cantilevers resolves different structural conformations of the DNA double helix. *Nano Lett.* 12: 3846–3850.

93. Ido S et al (2014) Immunoactive two-dimensional self-assembly of monoclonal antibodies in aqueous solution revealed by atomic force microscopy. *Nat. Mater.* 13: 264–270.

94. Custance O et al (2009) Atomic force microscopy as a tool for atom manipulation. *Nat. Nanotechnol.* 4: 803–810.

95. Fukuma T; (2020) Improvements in fundamental performance of in-liquid frequency modulation atomic force microscopy. *Microscopy (Oxf)* 69: 340–349.

96. Giessibl F J (2021) Probing the nature of chemical bonds by atomic force microscopy. *Molecules* 26: 4068.

97. Zhong Q et al (1993) Fractured polymer/silica fiber surface stud-ied by tapping mode atomic force microscopy. *Surf. Sci. Lett.* 290: L688–L692.

98. Meyer G and Amer N M (1988) Novel optical approach to atomic force microscopy. *Appl. Phys. Lett.* 53: 1045–1047.

99. Alexander S et al (1989) An atomic-resolution atomic-force microscope implemented using an optical lever. *J. Appl. Phys.* 65: 164–167.

100. Kindt J H et al (2004) Rigid design of fast scanning probe microscopes using finite element analysis. *Ultramicroscopy* 100: 259–265.

101. Ando T (2022) *High-Speed Atomic Force Microscopy in Biology* (Springer Berlin, Heidelberg).

102. Sulchek T et al (2002) Characterization and optimization of scan speed for tapping-mode atomic force microscopy. *Rev. Sci. Instrum.* 73: 2928–2936.

103. Kokavecz J et al (2006) Imaging bandwidth of the tapping mode atomic force microscope probe. *Phys. Rev. B.* 73: 155403.

104. Mahmood I A and Reza Moheimani S O (2009) Fast spiral-scan atomic force microscopy. *Nanotechnology* 20: 365503.

105. Yong Y K et al (2010) High-speed cycloid-scan atomic force microscopy. *Nanotechnology* 21: 365503.

106. Ando T; (2013) Molecular machines directly observed by high-speed atomic force microscopy. *FEBS Lett.* 587: 997–1007.

107. Ando T et al (2013) High-speed AFM and applications to biomolecular systems. *Annu. Rev. Biophys.* 42: 393–414.

108. Yamashita H et al (2009) Dynamics of bacteriorhodopsin 2D crystal observed by high-speed atomic force microscopy. *J. Struct. Biol.* 167: 153–158.

109. Miyagi A et al (2016) High-speed atomic force microscopy shows that annexin V stabilizes membranes on the second timescale. *Nat. Nanotechnol.* 11: 783–790.

110. Nievergelt A P et al (2018) High-speed photothermal off-resonance atomic force microscopy reveals assembly routes of centriolar scaffold protein SAS-6. *Nat. Nanotechnol.* 13: 696–701.

111. Fantner G E et al (2010) Kinetics of antimicrobial peptide activity measured on individual bacterial cells using high-speed atomic force microscopy. *Nat. Nanotechnol.* 5: 280–285.

112. Matusovsky O S et al (2019) High-speed AFM reveals subsecond dynamics of cardiac thin filaments upon Ca(2+) activation and heavy meromyosin binding. *Proc. Natl. Acad. Sci. U.S.A.* 116: 16384–16393.

113. Matusovsky O S et al (2021) Millisecond conformational dynam-ics of skeletal myosin II power stroke studied by high-speed atomic force microscopy. *ACS Nano* 15: 2229–2239.

114. Yokokawa M et al (2006) Fast-scanning atomic force microscopy reveals the ATP/ADP-dependent conformational changes of GroEL. *EMBO J.* 25: 4567–4576.

115. Heath G R and Scheuring S (2018) High-speed AFM height spectroscopy reveals micros-dynamics of unlabeled biomolecules. *Nat. Commun.* 9: 4983.

116. Matin T R et al (2020) Millisecond dynamics of an unlabeled amino acid transporter. *Nat. Commun.* 11: 5016.

117. Perrino A P et al (2021) Single molecule kinetics of bacteri-orhodopsin by HS-AFM. *Nat. Commun.* 12: 7225.

118. Radmacher M et al (1994) Direct observation of enzyme activity with the atomic force microscope. *Science* 265: 1577–1579.

119. Pelling A E et al (2004) Local nanomechanical motion of the cell wall of *Saccharomyces cerevisiae*. *Science* 305: 1147–1150.

120. García R (2010) *Amplitude Modulation Atomic Force Microscopy* (Wiley-VHC, Germany).

121. Martin Y et al (1987) Atomic force microscope-force mapping and profiling on a sub 100-Å scale. *J. Appl. Phys.* 61: 4723–4729.

122. Bustamante C and Keller D (1995) Scanning force microscopy in biology. *Phys. Today* 48: 32–38.

123. Fuentes-Perez M E et al (2013) AFM volumetric methods for the characterization of proteins and nucleic acids. *Methods* 60: 113–121.

124. Chen Y (2012) Elucidation and identification of double-tip effects in atomic force microscopy studies of biological structures. *J. Surf. Eng. Mater. Adv. Technol.* 02: 238–247.

125. Heath G R et al (2021) Localization atomic force microscopy. *Nature* 594: 385–390.

126. Rust M J et al (2006) Sub-diffraction-limit imaging by stochastic optical reconstruction microscopy (STORM). *Nat. Methods* 3: 793–796.

127. Betzig E et al (2006) Imaging intracellular fluorescent proteins at nanometer resolution. *Science* 313: 1642–1645.

128. Kasas S et al (2000) Simulation of an atomic force microscope imaging a moving protein. *Probe Microsc.* 2: 37–44.

129. Hall D and Foster A S (2022) Practical considerations for feature assignment in high-speed AFM of live cell membranes. *Biophys. Physicobiol.* 19: 1–21.

130. Miyagi A et al (2008) Visualization of intrinsically disordered regions of proteins by high-speed atomic force microscopy. *Chemphyschem* 9: 1859–1866.

131. Shibata M et al (2018) Oligomeric states of microbial rhodopsins determined by high-speed atomic force microscopy and circular dichroic spectroscopy. *Sci. Rep.* 8: 8262.

132. Shihoya W et al (2019) Crystal structure of heliorhodopsin. *Nature* 574: 132–136.

133. Araiso Y et al (2019) Structure of the mitochondrial import gate reveals distinct preprotein paths. *Nature* 575: 395–401.

134. Kishi K E et al (2022) Structural basis for channel conduction in the pump-like channelrhodopsin ChRmine. *Cell* 185: 672–689.e623.

135. Kusumi A et al (2005) Paradigm shift of the plasma membrane concept from the two-dimensional continuum fluid to the partitioned fluid: high-speed single-molecule tracking of membrane molecules. *Annu. Rev. Biophys. Biomol. Struct.* 34: 351–378.

136. Shimizu M et al (2022) An ultrafast piezoelectric Z-scanner with a resonance frequency above 1.1 MHz for high-speed atomic force microscopy. *Rev. Sci. Instrum.* 93: 013701.

137. Bozchalooi I S and Youcef-Toumi K (2014) Multi-actuation and PI control: a simple recipe for high-speed and large-range atomic force microscopy. *Ultramicroscopy* 146: 117–124.

138. Nievergelt A P et al (2015) Studying biological membranes with extended range high-speed atomic force microscopy. *Sci. Rep.* 5: 11987.

139. Miyagi A and Scheuring S (2018) A novel phase-shift-based amplitude detector for a high-speed atomic force microscope. *Rev. Sci. Instrum.* 89: 083704.

140. Umeda K et al (2021) Architecture of zero-latency ultrafast amplitude detector for high-speed atomic force microscopy. *Appl. Phys. Lett.* 119: 181602.

141. Fukuda S and Ando T (2021) Faster high-speed atomic force microscopy for imaging of biomolecular processes. *Rev. Sci. Instrum.* 92: 033705.

142. Amyot R et al (2022) Simulation atomic force microscopy for atomic reconstruction of biomolecular structures from resolution-limited experimental images. *PLoS Comput. Biol.* 18: e1009970.

143. Amyot R and Flechsig H (2020) BioAFMviewer: an interactive interface for simulated AFM scanning of biomolecular structures and dynamics. *PLoS Comput. Biol.* 16: e1008444.

144. Niina T et al (2021) Rigid-body fitting to atomic force microscopy images for inferring probe shape and biomolecular structure. *PLoS Comput. Biol.* 17: e1009215.

145. Niina T et al (2020) Flexible fitting of biomolecular structures to atomic force microscopy images via biased molecular simulations. *J. Chem. Theory Comput.* 16: 1349–1358.

146. Dasgupta B et al (2020) Reconstruction of low-resolution molecular structures from simulated atomic force microscopy images. *Biochim. Biophys. Acta. Gen. Subj.* 1864: 129420.

147. Kubo S et al (2020) Resolving the data asynchronicity in high-speed atomic force microscopy measurement via the Kalman Smoother. *Sci. Rep.* 10: 18393.

148. Fuchigami S and Takada S (2022) Inferring conformational state of myosin motor in an atomic force microscopy image via flexible fitting molecular simulations. *Front. Mol. Biosci.* 9: 882989.

149. Fuchigami S et al (2021) Case report: Bayesian statistical inference of experimental parameters via biomolecular simulations: atomic force microscopy. *Front. Mol. Biosci.* 8: 636940.

150. Fuchigami S et al (2020) Particle filter method to integrate high-speed atomic force microscopy measurements with biomolecular simulations. *J. Chem. Theory Comput.* 16: 6609–6619.

151. Matsunaga Y et al (2023) End-to-end differentiable blind tip reconstruction for noisy atomic force microscopy images. *Sci. Rep.* 13: 129.

152. Velankar S et al (2021) The protein data bank archive. *Methods Mol. Biol.* 2305: 3–21.

153. Brändén G and Neutze R (2021) Advances and challenges in time-resolved macromolecular crystallography. *Science* 373: eaba0954.

154. Guaita M et al (2022) Recent advances and current trends in cryo-electron microscopy. *Curr. Opin. Struct. Biol.* 77: 102484.

155. Amann S J et al (2023) Frozen in time: analyzing molecular dynamics with time-resolved cryo-EM. *Structure* 31: 4–19.

156. Takahashi H et al (2016) Temperature-controlled high-speed AFM: real-time observation of ripple phase transitions. *Small* 12: 6106–6113.

157. Matsui S et al (2018) Monitoring thermoresponsive morphological changes in individual hydrogel microspheres. *ACS Omega* 3: 10836–10842.

158. Ganser C and Uchihashi T (2019) Microtubule self-healing and defect creation investigated by in-line force measurements during high-speed atomic force microscopy imaging. *Nanoscale* 11: 125–135.

159. Chan F Y et al (2022) Tip-scan high-speed atomic force microscopy with a uniaxial substrate stretching device for studying dynamics of biomolecules under mechanical stress. *Rev. Sci. Instrum.* 93: 113703.

160. Nonaka S et al (2020) Molecular and functional analysis of pore-forming toxin monalysin from entomopathogenic bacterium *Pseudomonas entomophila*. *Front. Immunol.* 11: 520.

161. Fukuda S et al (2013) High-speed atomic force microscope combined with single-molecule fluorescence microscope. *Rev. Sci. Instrum.* 84: 073706.

162. Yoshida A et al (2018) Morphological changes of plasma membrane and protein assembly during clathrin-mediated endocytosis. *PLoS Biol.* 16: e2004786.